5

Ni-substituted (Fe_3C/Fe_3O_4)/C nanocomposites

5.1 Introduction

This chapter describes the structural, magnetic, biocompatible and catalytic behavior for nanocomposite for Ni-substituted (Fe_3C/Fe_3O_4)/C. Herein, the catalytic behavior of Fe_3C/C, as well as Fe_3C/Fe_3O_4/C is also discussed for comparison. The structural and morphological properties of the nanocomposites were established by x-ray diffraction and transmission electron microscope. X-ray photoelectron spectroscopy study was done to determine the oxidation states for the elements. MPMS and Mössbauer spectroscopy were utilized for understanding magnetic behavior. Further, the heating efficacy of these nanocomposite based ferrofluids were also evaluated at a field of 23 mT with a concentration of the 10 mg/mL. The biocompatibility of N3FOC was examined using SRB assay after the incubation of 48 h with A549 cell lines. The optical and photocatalytic activities of the nanocomposites were studied in detail. Further, two dyes methyl orange and p- nitrophenol were utilized to check performance of catalytic degradation under Fenton and photo-Fenton conditions. The optimum apparent catalytic reaction rate constant for Fe_3C/Fe_3O_4/C with p-nitrophenol and methyl orange were ~1.48 $x10^{-2}$ and 3.36 x 10^{-2} mol. $lit^{-1}min^{-1}$ respectively.

5.2 Results and discussion

5.2.1 Phase analysis

The X-ray diffraction patterns for the samples FC and FOC are shown in Fig. 5.1 (a). The peaks of the patterns were matched with the Fe_3C (JCPDS no. 65-2413) for sample FC but with Fe_3C (JCPDS no. 65-2413) and Fe_3O_4 (JCPDS no. 65-3107) for FOC. Furthermore, one major peak for graphitic carbon (JCPDS no. 89-8487) was also observed at 26.55º (002) in both the patterns. Figure 5.1 (b) represents the x-ray diffraction patterns for Ni-substituted nanocomposites namely N1FOC, N3FOC and N5FOC (for x = 0.1, 0.3 and 0.5) respectively. For all the samples, the peaks corresponded to Fe_3C and Fe_3O_4 phases. Similar to undoped one, these samples also had graphitic carbon. The percentage compositions of the phases in the nanocomposite were assessed using X'pert high score plus software and the values are shown in Figs. 5.1 (a) and 5.1 (b). It is noticeable that the Fe_3C phase was relatively more in the unsubstituted sample but its concentration diminished continually with enhanced Ni substitution (Fig. 5.1 N1FOC through N5FOC). It indicates that Ni ions are more favorable for oxide formation than the carbide phase. However, beyond this concentration (i.e. $x > 0.5$), the sample had an additional NiO phase (figure not given). Therefore, further characterization was not done. Moreover, it was quite tedious to find out the exact occupancy of Ni in Fe_3C or Fe_3O_4 phase.

The crystallite size of both the phases (Fe_3C and Fe_3O_4) were calculated with the help of Scherrer's equation, and found to be around 5-11 nm (Table 5.1). There was only a slight variation in the crystallite size with increased Ni substitutions for both phases. The modification of the lattice parameter for both phases (*viz.* Fe_3C and Fe_3O_4) with

enhanced Ni content is presented in Table 5.1. XRD revealed that there was a minor decrement in the lattice parameter for both phases with improved Ni concentration (Table 5.1). This was also revealed from XRD patterns which have shown a minute displacement towards right. It could be attributed to the difference in the atomic radii of Fe and Ni as well as ionic radii of Fe^{2+}, Fe^{3+} and Ni^{2+} ions. The reported values for ionic radii of Fe^{2+} and Fe^{3+} ions at tetrahedral sites are 0.77 and 0.63 Å respectively and at octahedral voids are 0.92 and 0.79 Å, respectively [10].

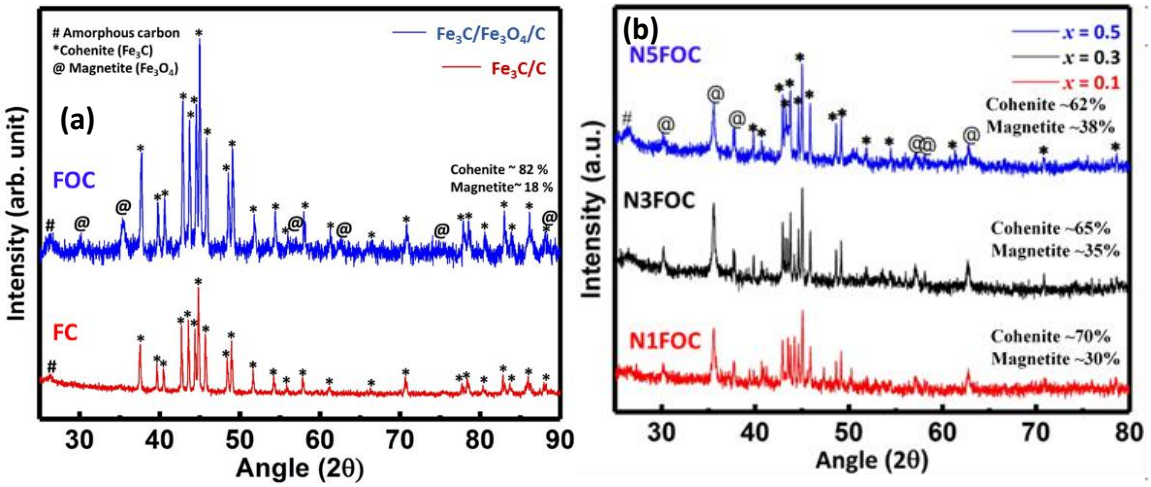

Figure 5.1: X-ray diffraction patterns for the nanocomposites (a) FC and FOC and (b) N1FOC, N3FOC and N5FOC.

In contrast, Ni^{2+} ions have ionic radii of 0.69 and 0.83 Å at tetrahedral and octahedral sites respectively. This validates the continuous reduction in the lattice parameter for Fe_3O_4 phase. Similarly, the metallic atomic radii for Fe and Ni are 1.26 and 1.24 Å and hence the increased incorporation of Ni even reduced the lattice parameter of Fe_3C phase.

Table 5.1: Details of the structural parameters obtained from Rietveld refinement by automatic Fullprof Match! Software.

Sr. no.	Sample	Lattice parameter (a, b, c) (Å)		Angles (°)	Crystallite size (nm)	
		Fe_3C	Fe_3O_4	α, β, γ	Fe_3C	Fe_3O_4
1	FC	5.0929, 6.7467, 4.5285	---	90	~5	~6
2	FOC	5.0928, 6.7466, 4.5281	8.365	90	~7	~8
3	N1FOC	5.0922, 6.744, 4.528	8.362	90	~8	~7
4	N3FOC	5.0917, 6.7435, 4.526	8.360	90	~8	~7
5	N5FOC	5.0915, 6.7431, 4.5257	8.358	90	~10	~11

5.2.2 Morphological analysis

Transmission electron microscopy was utilized to get information about the particle size, nature of its distribution and morphology. The bright-field micrograph of the sample FC is shown in Fig. 5.2 (a).

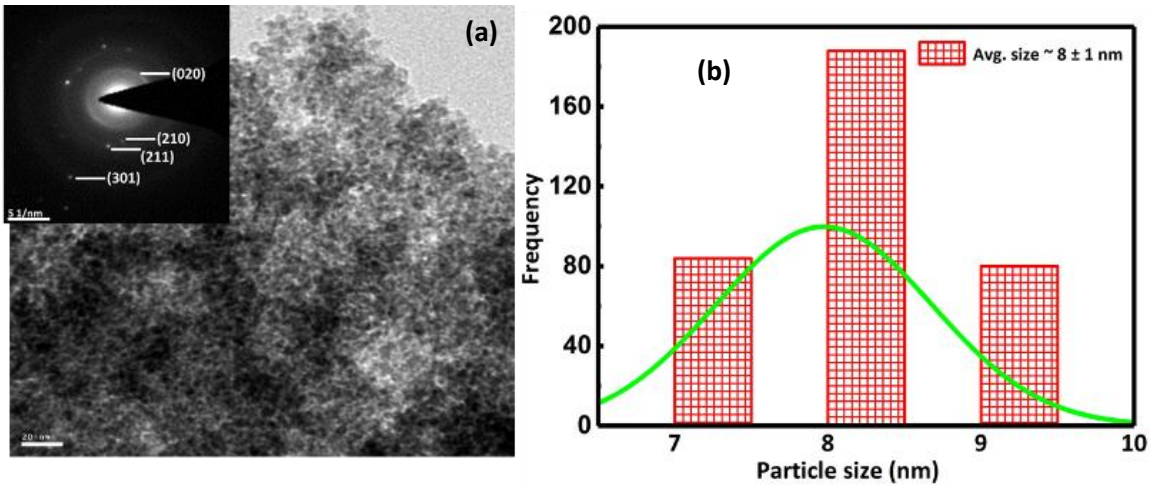

Figure 5.2. TEM analysis of the sample FC a) bright field micrograph, b) histogram of the particle distribution.

It showed homogeneously distributed particles in the size range of ~7-10 nm and an average size of ~8±1 nm. The size of the particles was measured (taking ~ 350 particles) with the help of ImageJ software and presented as a histogram in Fig. 5.2 (b).

The selected area electron diffraction (SAED) pattern of the sample FC acquired diffused rings, which could be ascribed for extremely finer particles (inset of Fig. 5.2 a). The planes (020), (210), (211), and (301) evaluated from the rings or the spots confirmed the formation of the Fe_3C phase (inset of Fig. 5.2 a).

Similarly, the TEM micrograph for the nanocomposite N3FOC in Fig. 5.3 (a) was used to deduce the morphology of the particles. The micrograph exhibits the clusters of nanoparticles. However, it was challenging to get the size of individual nanoparticles. The ring SAED pattern for the sample is shown as the inset of Fig. 5.3 (a), which represents its polycrystalline nature. Employing the ImageJ software, the measured d-spacing values were 4.8, 2.96 and 2.53 nm, which confirmed the planes (111), (220) and (311) respectively for Fe_3O_4 phase.

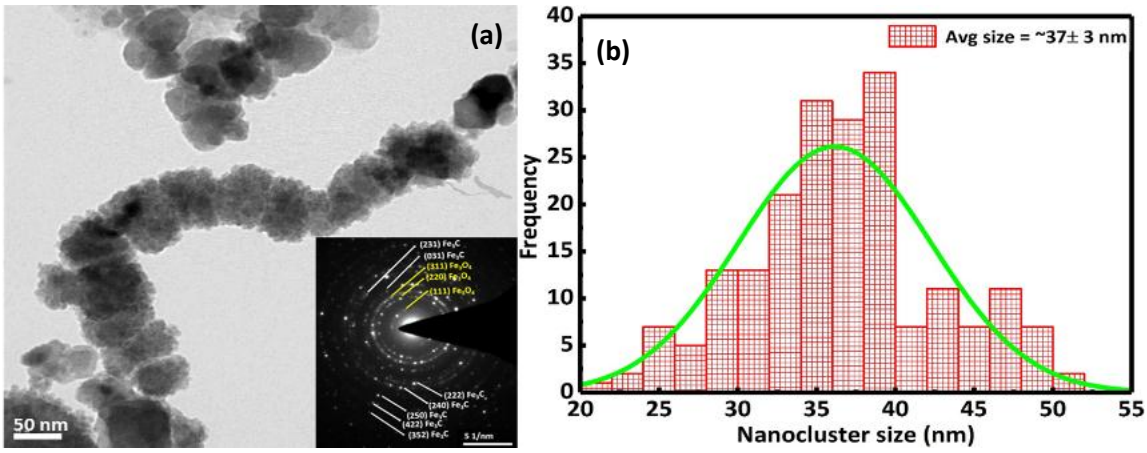

Figure 5.3: TEM analysis of the nanocomposite N3FOC a) bright field micrograph, b) SAED pattern and c) histogram of nanoclusters size.

Besides, the d spacing values were measured as 2.02, 1.57, 1.51, 1.39, 1.19, 1.058, and 0.95 nm for Fe_3C planes (031), (231), (222), (240), (250), (422) and (352) respectively. However, no separate d-spacing values were observed either for NiO or

any other phases. Since, the size of the individual nanoparticles was too low to measure and hence the size of each nanoclusters was estimated using ImageJ software (considering > 250 clusters). The nanoclusters had a size in the range of 15-50 nm and the average size was around 35 ±1 nm which is designated as histogram in Fig. 5.3 (b).

5.2.3 XPS analysis

X-ray photoelectron spectroscopy of the sample N5FOC is shown in Fig. 5.4, which suggests the chemical states of the elements present. The XPS spectra confirmed the coexistence of Fe, C, Ni and O in N5FOC nanocomposite. The XPS spectrum for Fe2p was deconvoluted into five peaks, which is presented in Fig. 5.4 (a). The peak at 710.73 eV represents the central $Fe2p_{3/2}$ peak due to Fe^{3+} oxidation states of Fe. Another two peaks at 713.17 and 725.22 eV ascribed to Fe2p3/2 and Fe2p1/2 respectively for Fe atoms. Moreover, two satellite peaks were also detected at 718.67 and 733.57 eV, which can be ascribed as F2p3/2 and Fe2p1/2 for Fe^{3+} and Fe^{2+} respectively. The presence of Fe^{2+} and Fe^{3+} is due to Fe_3O_4 phase whereas the elemental Fe indicates Fe_3C phase. The XPS spectrum for C1s was decoupled into two peaks which are shown in Fig. 5.4 (b). The binding energies for these two peaks were detected at 284.67 and 285.89 eV due to C-C and C-O-C bondings respectively. Similarly, the XPS spectrum for the Ni2p was deconvoluted into four peaks (Fig. 5.4 c). Out of these, the two had values of 855.84 and 873.64 eV representing for the spin-orbit doublets for Ni2p3/2 and Ni2p1/2 respectively. Another two peaks signify the shakeup satellite peaks at 861.81 and 879.8 eV for Ni^{2+} state. Likewise, Fig. 5.4 (d) represents the O1s spectrum, which is well fitted with two peaks. The peaks at the binding energies 530 and 531.5 eV may be ascribed for M-O and M-C-O bondings.

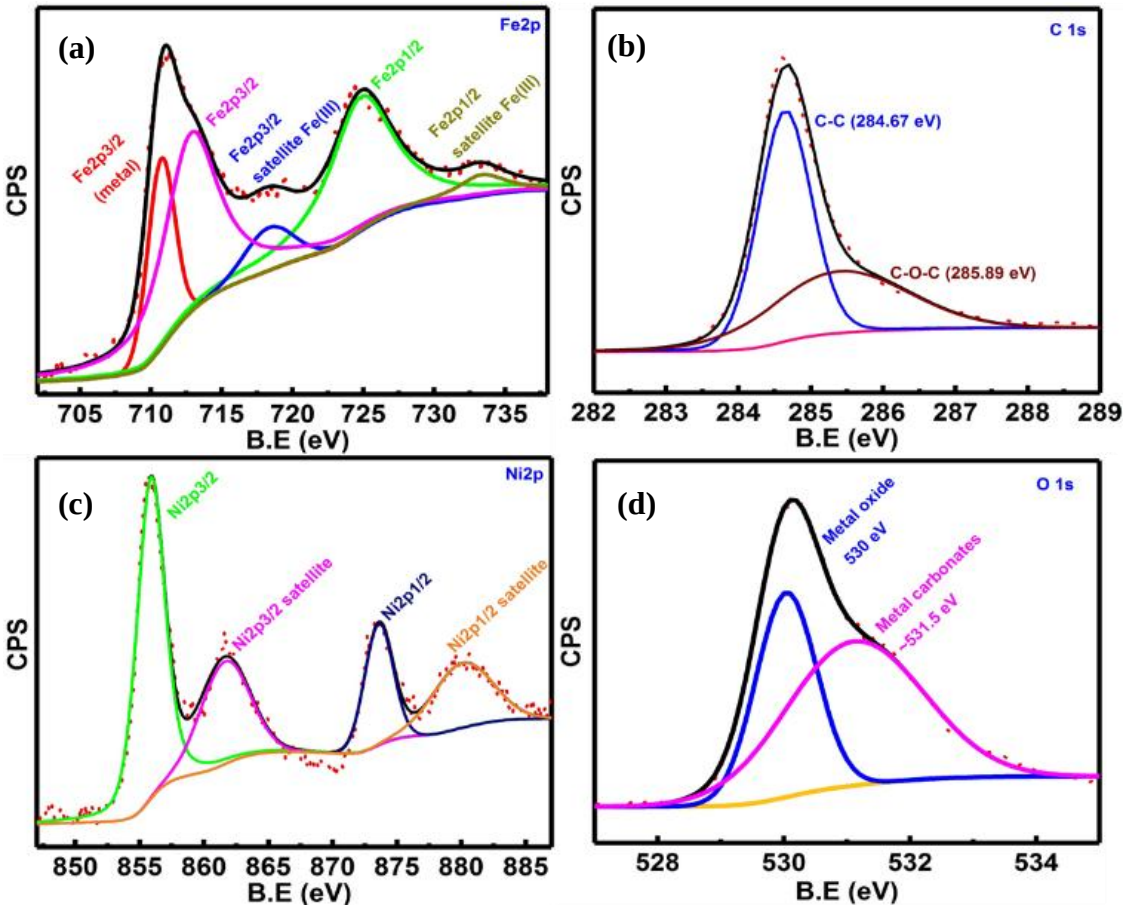

Figure 5.4: XPS spectra for sample N5FOC nanocomposite a) Fe2p, b) C1s, c) Ni2p and d) O1s.

5.2.4 Mössbauer spectroscopy

The Mössbauer spectra of all the Ni-substituted nanocomposites (*viz*. N1FOC, N3FOC and N5FOC) were recorded under ambient conditions and are displayed in Fig. 5.5. The obtained parameters such as the hyperfine field (B_{hf}), isomer shift (δ), quadruple splitting (Δ) and relative area (R_A) after fitting of the spectra are listed in Table 5.2. Fig. 5.5 (a) represents the Mössbauer spectrum for N1FOC, which was fitted with four sextets and one doublet. The sextets A and B denote two different sites for Fe in the orthorhombic unit cell of Fe_3C and the B_{hf} values were 20.69, 19.94 T (Table 5.2). In contrast, the other two sextets indicate two different sites for Fe in the spinel Fe_3O_4 phase.

For these two sextets, the B_{hf} values 49.47 and 45.13 T corresponding to the tetrahedral and octahedral sites respectively were noticed (Table 5.2) [10]. For both the phases, the obtained values were lesser than the bulk values but similar to some of the reported values. However, the reduced hyperfine field values for Ni-substituted carbide might also be due to the formation of antiferromagnetic coupling between Ni and Fe. For both the phases, the magnitude of the quadruple splitting and isomer shifts values modified minutely due to the incorporation of Ni and nanoscale sized particles. Furthermore, the relative area values suggest that the compositions of carbide and oxide phases were about 69 and 24% respectively (Table 5.2). The remaining part (i.e. 7 %) for the doublet designates the superparamagnetic component. This may be because of extremely finer particles of both the phases (i.e. carbide and oxide). As Ni content improves, for the N3FOC sample, the B_{hf} values for the sextets of the carbide phase decreased slightly (Table 5.2). However, for the oxide phase, the sextets have similar B_{hf} values as that of the earlier sample (i.e. N1FOC, Table 5.2). Nevertheless, no significant modification in the IS values for the two phases was noticed. The relative concentration for carbide, oxide and superparamagnetic components in N3FOC was around 65, 24 and 11%, respectively (Table 5.2). Besides, the IS values reduced for all the sextets of this sample. It may be attributed to the presence of a large concentration of Ni in this sample. Similarly, for N5FOC sample, the estimated concentration was approximately 62, 28 and 10% for carbide, oxide and superparamagnetic part, respectively (Table 5.2). Here, it can be inferred that the concentration of carbide phase reduced whereas the oxide content increased with improving Ni content (Table 5.2). This observation was also supporting the concentration of the phases as evaluated by X'pert high score plus software.

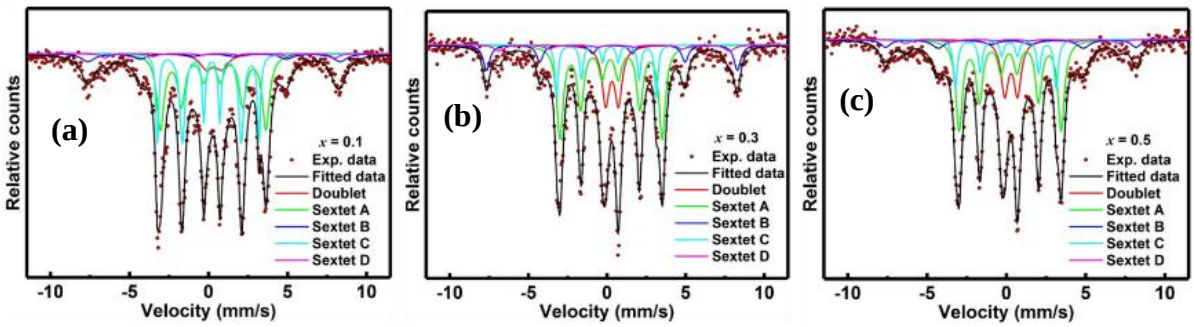

Figure 5.5: Mössbauer spectroscopy of the samples N1FOC, N3FOC and N5FOC nanocomposite.

Similarly, for N5FOC sample (Fig. 5.5 c), B_{hf} value for the sextet A (carbide phase) reduced, but for the sextet B it remained almost unaltered (Table 5.2). This suggests that Ni might have got placed more at one preferred site in the carbide phase. In contrast, for the oxide phase, the B_{hf} value for octahedral sites remained almost unchanged, but a significant decrement was noticed for tetrahedral sites (Table 5.2). Besides, the IS values reduced for all the sextets of this sample. It may be attributed to the presence of a large concentration of Ni in this sample. The estimated concentration was approximately 62, 28 and 10% for carbide, oxide and superparamagnetic part, respectively in this sample (Table 5.2). Here, it can be inferred that the concentration of carbide phase reduced, but the oxide phase improved with increased Ni content in the sample (Table 5.2). This observation was supporting the concentration of the phases evaluated by X'pert high score plus software (Fig. 5.5).

Table 5.2: Summary of the Mössbauer magnetic hyperfine structural parameters for all samples after fitting.

Sample	Iron site	Hyperfine field (B_{hf}) T ± 0.01	Quadruple splitting, (Δ) mm/s ± 0.02	Isomer shift (δ) mm/s ± 0.01	Outer line width, (Γ) mm/s	Relative Area (R_A) ± 0.03 %	χ^2
N1FOC (x = 0.1)	*Sextet A*	20.69	0.985	0.247	0.97	51	1.3
	Sextet B	19.94	-0.23	0.079	0.22	18	
	Sextet C	49.47	0.046	0.317	1.03	19	
	Sextet D	45.13	0.022	0.71	0.65	5	
	Doublet	-	0.985	0.34	0.97	7	
N3FOC (x = 0.3)	*Sextet A*	20.15	0.63	0.22	0.49	57	1.6
	Sextet B	19.65	0.243	0.073	0.25	8	
	Sextet C	49.46	-0.029	0.32	0.57	16	
	Sextet D	45.4	-0.083	0.49	0.75	8	
	Doublet	-	0.81	0.3077	0.55	11	
N5FOC (x = 0.5)	*Sextet A*	19.94	0.074	0.19	0.49	52	1.2
	Sextet B	19.69	-0.24	0.07	0.3	10	
	Sextet C	48.94	-0.0015	0.27	0.77	23	
	Sextet D	41.79	-0.030	0.38	0.75	5	
	Doublet	-	0.812	0.288	0.55	10	

5.2.5 Magnetic properties analysis

Magnetic properties of the nanocomposites were evaluated using magnetic properties measurement system (MPMS). Fig. 5.6 (a) represents the magnetization (M) *vs.* field (H) curves for the samples N1FOC, N3FOC and N5FOC at room temperature. All the samples show a hysteresis loop, which refers to their Ferro- or ferrimagnetic behavior (inset of Fig 5.6 a). The M_S value for the FC sample was 68 Am^2/kg which was lower than its bulk sample (~130 Am^2/kg) [25]. It could be accomplished to the submicroscopic sized particles and the presence of carbon. Further, the M_S value for the

FOC sample was obtained to be 60 Am^2/kg. The lower value of magnetization for FOC than the FC sample may be attributed to the presence of the oxide phase. For Ni-substituted samples *viz.* N1FOC, N3FOC and N5FOC, the M_S value was 58, 47 and 44 Am^2/kg, respectively (Fig. 5.6 b). The constant reduction in the M_S value with increased Ni concentration may be associated with enhanced oxide content. It was validated from XRD and Mossbauer analysis. Nevertheless, the incorporation of Ni in the nanocomposite would also have contributed to the decrement in the M_S value due to antiferromagnetic coupling between Fe and Ni in Fe_3C. However, it is challenging to comment on the effect of Ni on the magnetization of individual phases (carbide and oxide). It is because of the lack of information about the distribution of Ni in two phases. Moreover, the Ni incorporation in the octahedral sites of Fe_3O_4 generally reduces its magnetization value. Figure 5.6 (b) represents variation in the coercivity (H_C) and remanence (M_r) values for the nanocomposites with increased Ni-substitution. The optimum H_C and M_r values were 12.5 mT and 4.7 Am^2/kg and these values continuously reduced with improved Ni-substitution.

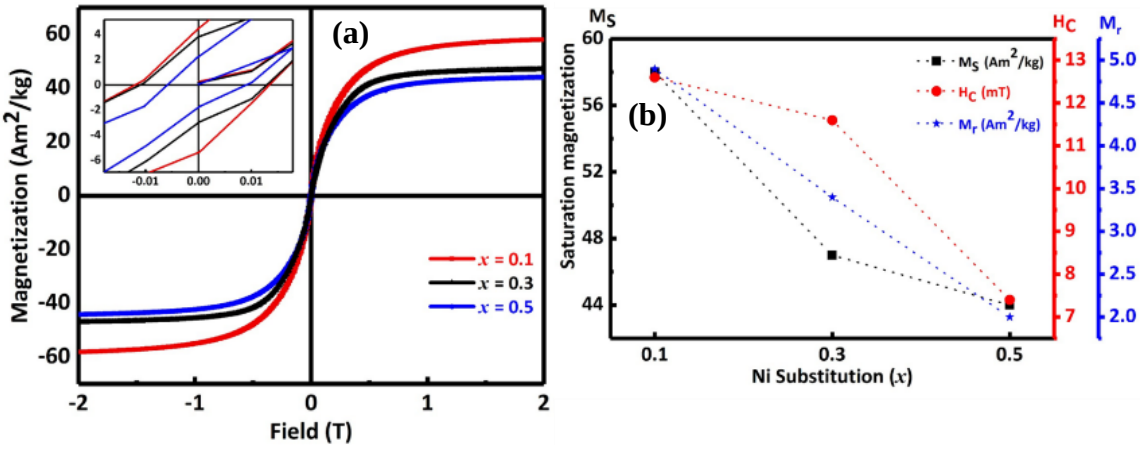

Figure 5.6: (a) Magnetization *vs.* field curves and (b) the variation in the Ms, Hc and M_r values with Ni substitution of nanocomposites N1FOC, N3FOC and N5FOC.

5.2.6 Heating ability

The performance of induction heating in the presence of external field (*viz.* 23 mT and 261 kHz) by the ferrofluids of nanocomposites is shown in Fig. 5.7. The aqueous ferrofluids were prepared using polymer F127 (13%w/v) and the concentration of MNPs in the ferrofluid was 10 mg/mL for each. The Fig. 5.7 a represents the plots of temperature rise w.r.t time. All the ferrofluids shown continuous temperature growth with increased duration (Fig. 5.7 a).

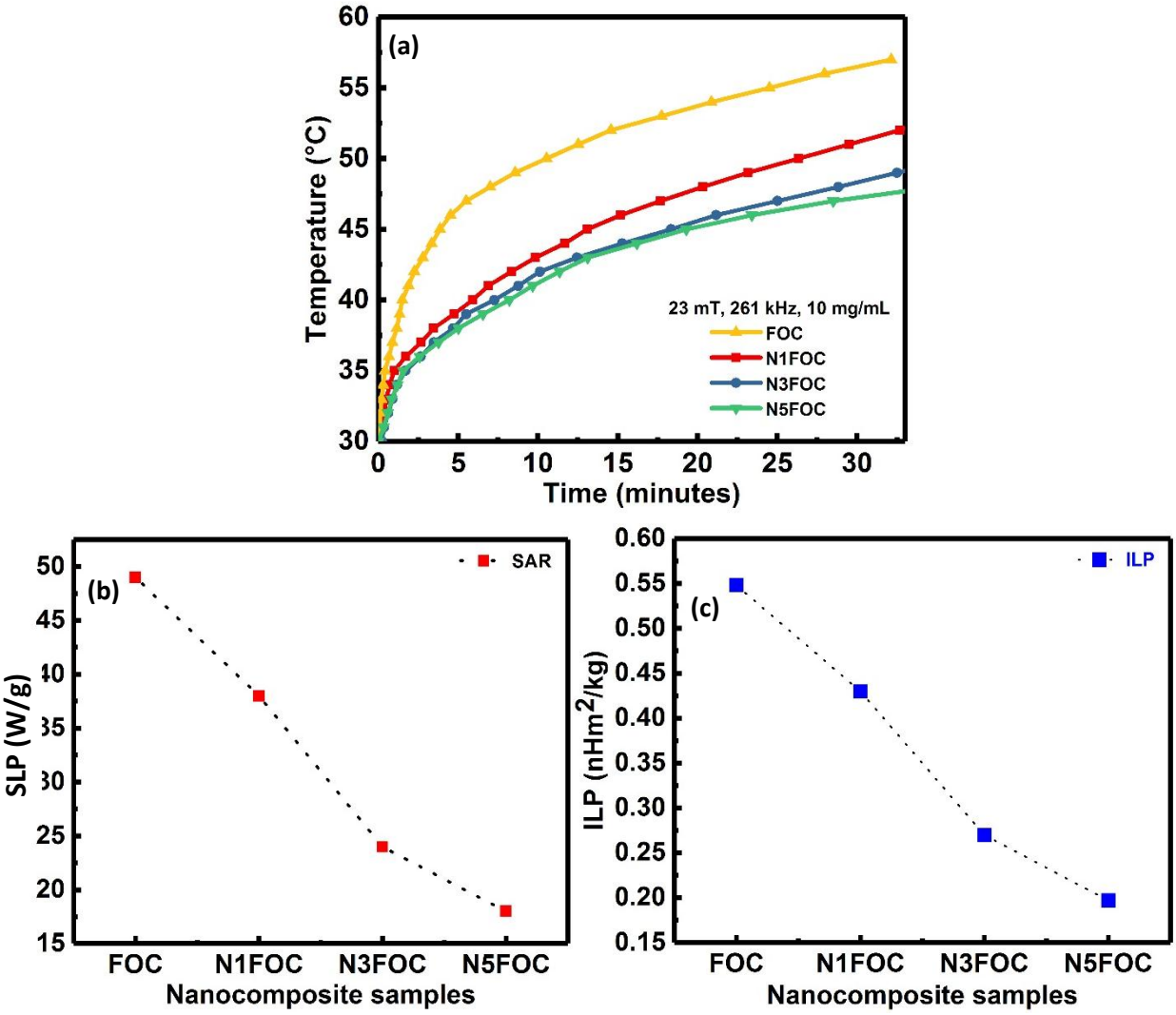

Figure 5.7: The induction heating behavior for the ferrofluids (FOC, N1FOC, N3FOC and N5FOC) (a) Time *vs.* temperature plots, (b) SLP values and (c) ILP values.

It was noticed that the initial heating rate for all the ferrofluids were relatively faster but the rate reduced at later stage. The time required to attain the therapeutic temperature (42 ºC) was 135, 500, 607, and 681 s for the FOC, N1FOC, N3FOC and N5FOC samples respectively. It can be observed that FOC took less time due to its higher M_S value which was accomplished to the higher proportion of carbide phase in it (Figs. 5.1 a, 5.6 and 5.7 a). Further, the samples with higher Ni content displayed slower heating rate and it might be due to their reduced M_S values (Figs. 5.6 and 5.7 a). Further, the heating performance of these samples as calculated in terms of SLP values is presented in Fig. 5.7 b. The SLP values were estimated to be as 49, 38, 24 and 18 W/g for the ferrofluids of FOC, N1FOC, N3FOC and N5FOC respectively. The optimum SLP value was for FOC sample because of its higher initial heating rate. Similarly, ILP values of these ferrofluids were also calculated which represents the intrinsic properties of the MNP_S (Fig. 5.7 c). The ILP values were 0.548, 0.43, 0.27 and 0.197 nHm^2/kg for the ferrofluids of FOC, N1FOC, N3FOC and N5FOC respectively. Similar to SLP values, the optimum ILP magnitude was observed for FOC sample. The observed SLP as well as ILP values were comparable to that of some of the reported values for the magnetic iron oxides samples. Therefore, it can be argued that these nanocomposites also have significant potential for the application of MHT.

5.2.7 Cytotoxicity studies

The in-vitro study to determine the compatibility of bare particles of Ni substituted sample (e.g. N3FOC) was performed with A549 cell. The percentage cells viability with this nanocomposite after 48 h of treatments is shown in Fig. 5.8. The

approximate % cell viability with improving concentrations of MNPs such as 0.1, 0.5, 1, 1.5, 2, 2.5 and 3 mg/mL was found to be 94, 84, 75, 73, 68, 66, and 60 respectively (Fig. 5.8 a). The % cell viability contineously diminished with increased concentration of MNPs. The observation suggests that the concntration up to 0.5 mg/mL may be consider as compatible. Nevertheless, only Fe_3C sample was compatible up to 1 mg/mL after 48 h (section 3.2.8). The reduced comptibility for the sample may be due to the presence of the Ni which is relatively more toxic than Fe. The fluorescence micrograph of the A549 cells treated with 0.1 mg/mL of MNPs for 24 h further suggests normal morphology for the treated cells (Fig. 5.8 b). There was no alteration in their morphologies due to physical and chemical interactions with the membrane of the cells. Thus, sample N3FOC may be assumed to be biocompatible upto to 0.5 mg/mL and can be analysed further.

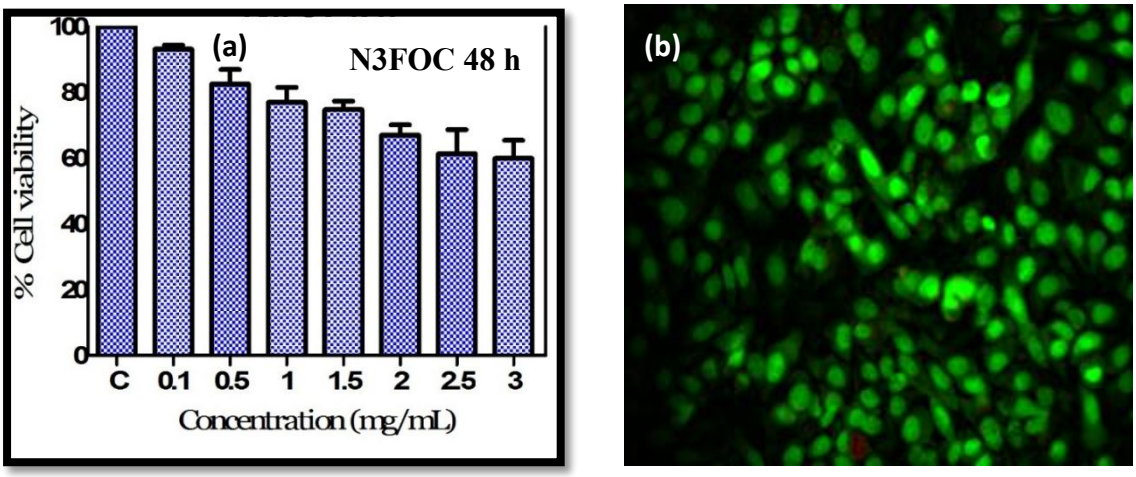

Figure 5.8: *In-vitro* study of bare N3FOC nanocomposite with A549 lung cancer cell lines: a) % cell viability with varying concentrations 0.1, 0.5, 1, 1.5, 2, 2.5 and 3 mg/mL and b) Fluorescence imaging after stained with acridine orange.

5.2.8 Band gap analysis

The knowledge of the band gaps in semiconductor composite materials is essential to conjecture the possible photocatalysis mechanism involved. Fig. 5.9 shows the Tauc plots constructed using solid-state UV-visible absorbance data for the composites reported here. The Tauc plots give the behavior of the molar absorption coefficient (α) and the photonic energy ($h\vartheta$) through equation (1) [83, 88].

$$(\alpha h\vartheta)^{1/n} = (h\vartheta - E_g) \quad \text{.....1}$$

where n = ½ for indirect transitions and 2 for direct transition.

The intercept of the plot between $(\alpha h\vartheta)^{1/n}$ and $h\vartheta$ gives the band gap, E_g. The estimated values of E_g for FC, FOC, N1FOC, N3FOC and N5FOC were 1.16, 1.55, 1.67, 1.7 and 1.76 eV respectively (Fig. 5.9). The continuous rise in the band gap may be attributed to the consistent rise in the concentration of Ni or oxide phase in the nanocomposites.

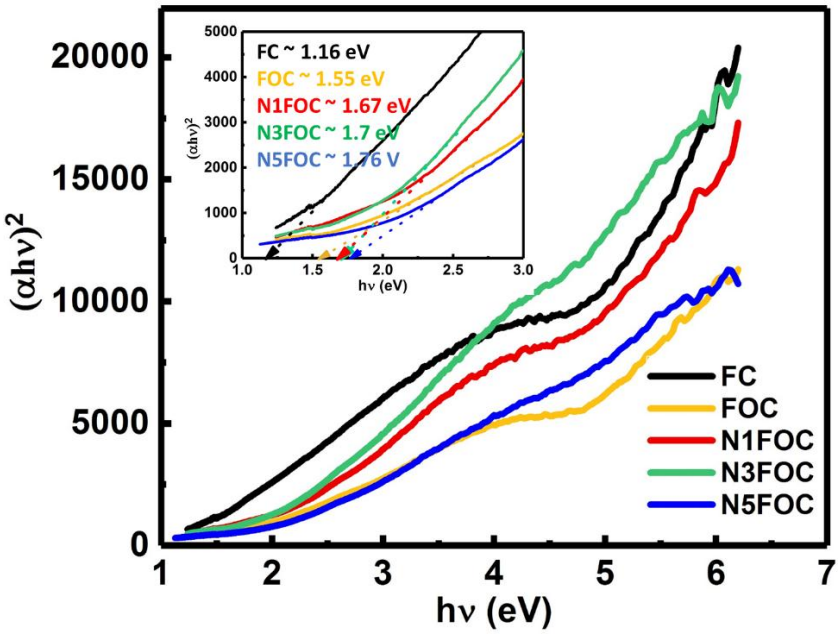

Figure 5.9: Tauc plots of the nanocomposites (FC, FOC, N1FOC, N3FOC and N5FOC) for the direct transitions and inset shows their direct bandgaps.

5.2.9 Fenton and photo-Fenton degradation of PNP

Figure 5.12 compares the kinetics of degradation of PNP under Fenton conditions over different nanocomposite particles (*viz.* FC, FOC, N1FOC, N3FOC and N5FOC). The PNP Fenton degradation over all nanocomposites followed first order kinetics. Figures 5.10 and 5.11 show the change in the UV-visible spectra of aqueous solution of PNP under Fenton and photo Fenton condition over FOC and N5FOC composite nanoparticles respectively. In Fig. 5.10 (a), all the PNP peaks decreased simultaneously with time indicating complete degradation. But the rate of degradation was much slower over N5FOC and there was negligible change in its UV-visible peak even after 60 minute of reaction time. Thus, Ni-doping in the catalyst drastically reduced the rate of Fenton PNP degradation. As it is well known, the heterogeneously catalyzed Fenton reaction over Fe_3O_4 utilizes the mixture of Fe^{2+} and Fe^{3+} ions present in it. In each catalytic cycle the Fe^{2+} get oxidized to Fe^{3+} species due to the reduction of H_2O_2.

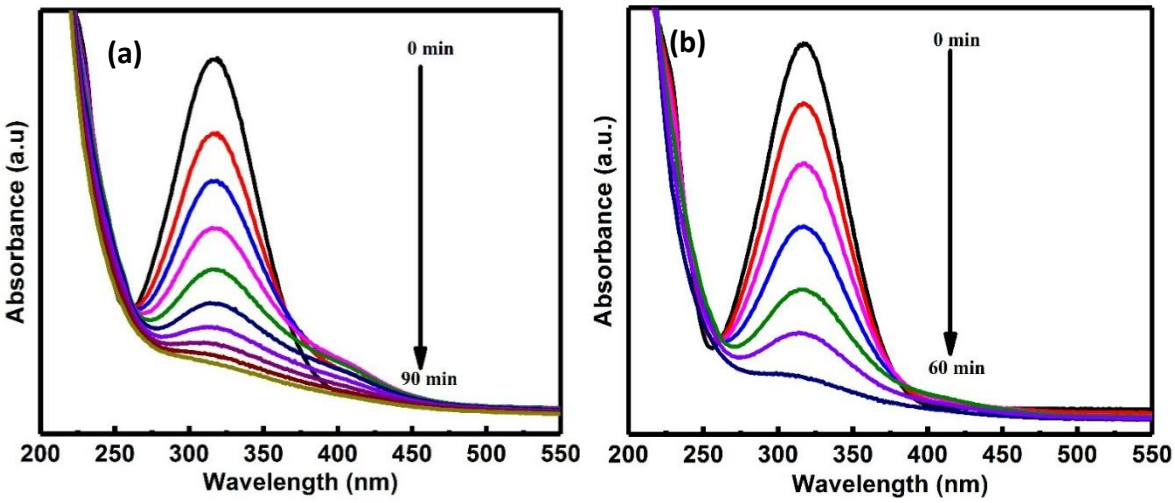

Figure 5.10: UV- Vis spectra of degradation of PNP using FOC catalyst under (a) Fenton and (b) Photo Fenton condition.

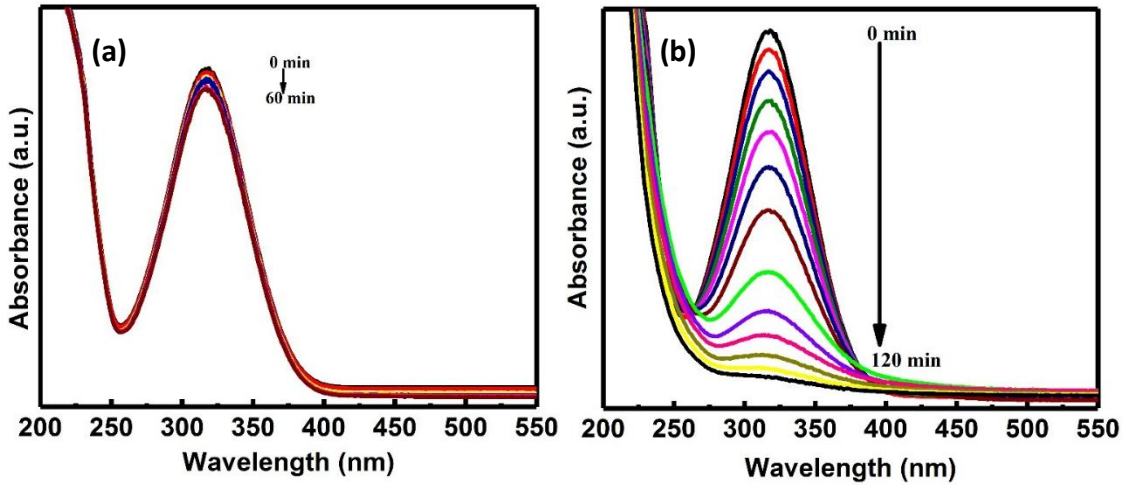

Figure 5.11: UV- Vis spectra of degradation of PNP using N5FOC catalyst under (a) Fenton and (b) Photo Fenton condition.

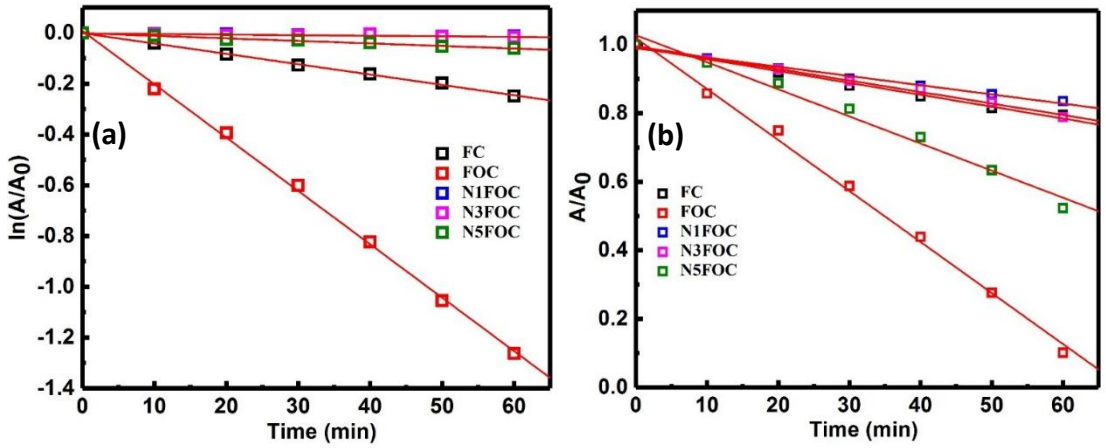

Fig. 5.12. Catalytic kinetics plots of PNP degradation at λ_{max} 317 nm under (a) Fenton and (b) Photo Fenton condition.

In contrast, the XRD and XPS results (Figs. 1.1 b and 5.4) for all Ni substituted nanocomposites indicate the replacement of Fe^{2+} ions by Ni^{2+} in Fe_3O_4. Since, Ni^{2+} ions cannot get oxidized further and hence its increased concentration continuously reduces the catalytic activity these nanocomposites. A comparison of figures 5.10 (a) (Fenton) and 5.10 (b) (PNP photo-Fenton on FOC) demonstrates the time for complete degradation which reduced to 60 minutes under photo-Fenton conditions. The PNP

Fenton degradation over N5FOC was nearly negligible (Fig. 5.11 a) but the UV-visible spectra of PNP photo-Fenton on N5FOC (Fig. 5.11 b) showed complete degradation after 120 minutes of reaction time. Thus, cool white LED visible light irradiation led to significantly enhanced kinetics of PNP Fenton degradation over doped as well as undoped nanocomposites. Moreover, the photo-Fenton PNP degradation followed zero-order kinetics, contrary to reaction under Fenton condition. The change in reaction kinetics order indicated a change in the catalytic mechanism due to light irradiation.

Figure 5.12 (b) gives the zero-order photo-Fenton kinetics plots of PNP degradation over undoped and doped composite nanoparticles. Despite the increase in the rate of PNP degradation under photo-Fenton conditions, the kinetics was faster over FOC than over Ni-doped samples. Another vital observation is that, among the Ni-doped nanocomposites, the kinetics of degradation becomes faster with enhanced percentage of doping. Thus, N5FOC displayed the highest rate of photo-Fenton PNP degradation among the Ni-doped nanocomposites. Table 5.3, gives the first order and zero order rate constants for Fenton and photo-Fenton degradation of PNP in its aqueous solution. Note that only the rate constants of reactions following the same order can be compared. Therefore, first order Fenton reaction rate constants can only be compared among themselves and similarly for the zero-order rate constants of the photo-Fenton cases.

Table 5.3: The apparent reaction rate constant for Fenton degradation and photo-Fenton degradation of PNP in presence of catalyst.

Catalyst	Apparent reaction rate constant for Fenton degradation of PNP (min^{-1})	Apparent reaction rate constant for photo-Fenton degradation of PNP (mol $lit^{-1}min^{-1}$)
FC	4.07×10^{-3}	3.4×10^{-3}
FOC	2.1×10^{-2}	1.48×10^{-2}
N1FOC	2.37×10^{-4}	2.6×10^{-3}
N3FOC	2.27×10^{-4}	3.3×10^{-3}
N5FOC	1×10^{-3}	7.9×10^{-3}

5.2.10 Fenton and photo-Fenton degradation of MO

Figure 5.15 (a) gives the kinetics of degradation of MO over various nanocomposites such as FC, FOC, N1FOC, N3FOC and N5FOC under Fenton conditions. Similar to the PNP Fenton case (Fig. 5.12 a), here also we find that Fenton degradation followed first order kinetics, though photo-Fenton conditions led to a zero order reaction (Fig. 5.12 b). Figures 5.13 (a) and 5.14 (a) display the UV-visible spectra showing a decrease in the MO absorbance maximum intensity with time over the FOC and N5FOC nanocomposites, respectively, under Fenton conditions. While the change in MO concentration with time was significant on FOC, there was almost negligible MO degradation over N5FOC in 50 minutes reaction time. The latter can again be attributed to Ni-doping impeding the H_2O_2 Fenton reduction mechanism. Fig. 5.15 (b) shows the MO degradation kinetics over Ni-doped and undoped nanocomposites under photo-Fenton settings. First of all, it was observed that in the photo-Fenton case all MO degradations followed zero order kinetics. Then the degradation over FOC under cool

white LED visible light is appreciably faster than that under plain Fenton conditions. Complete degradation occurred in only 30 minutes, compared to more than 60 minutes required for the same in absence of any light on the FOC catalyst (Fig. 5.14 a). In addition to this, the MO degradation over FOC was faster than that observed on any Ni-doped nanocomposites. Whereas the Fenton MO degradation over N5FOC was nearly negligible, the oxidation of MO under photo-Fenton environment was significantly quicker (Fig. 5.14 b).

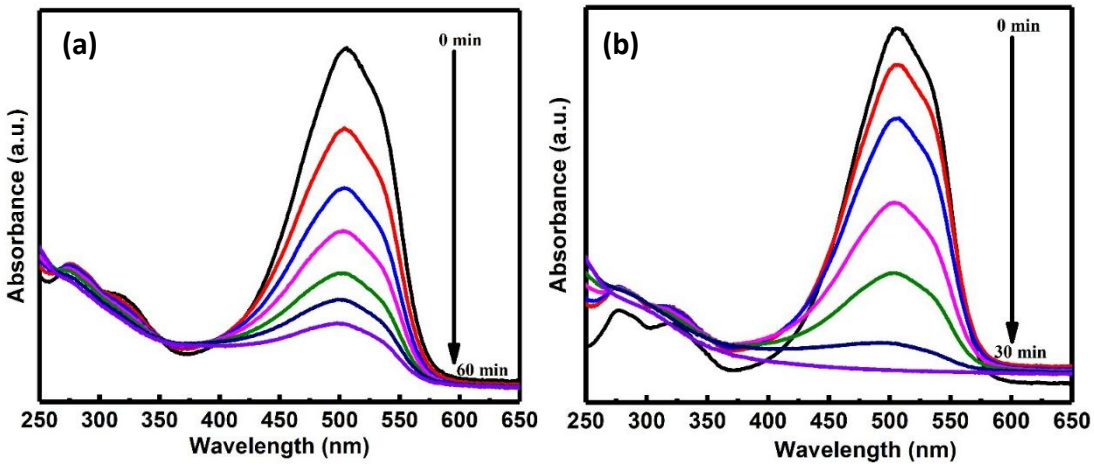

Figure 5.13: UV- Vis spectra of degradation of PNP using FOC catalyst under (a) Fenton and (b) Photo Fenton condition.

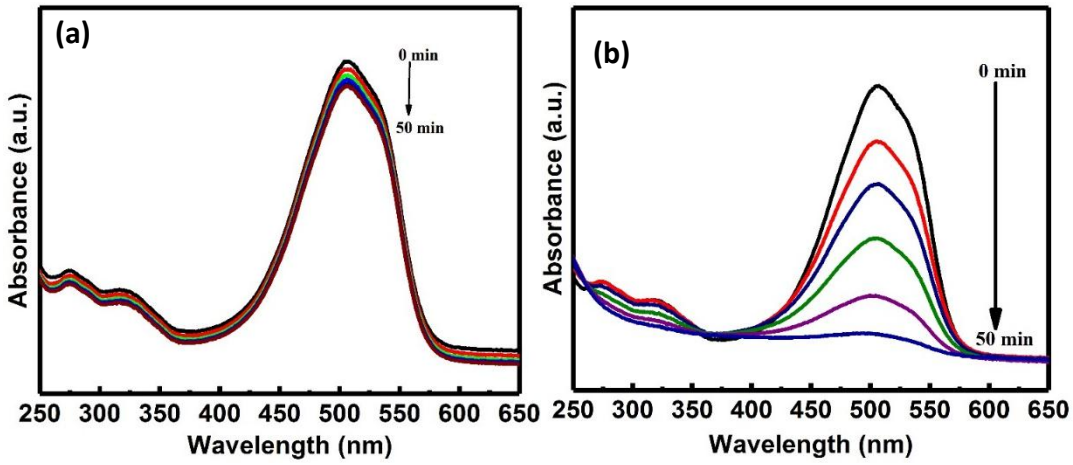

Figure 5.14: UV- Vis spectra of degradation of MO using N5FOC catalyst under (a) Fenton and (b) Photo Fenton condition.

The first column of Table 5.4 arranges the first-order rate constant values found for Fenton MO oxidation reactions. Similarly, the second column of this table indicates the values of zero-order rate constants when the reaction took place under cool white LED visible light. As mentioned earlier, one can only compare the rate constant values of only reactions with same order.

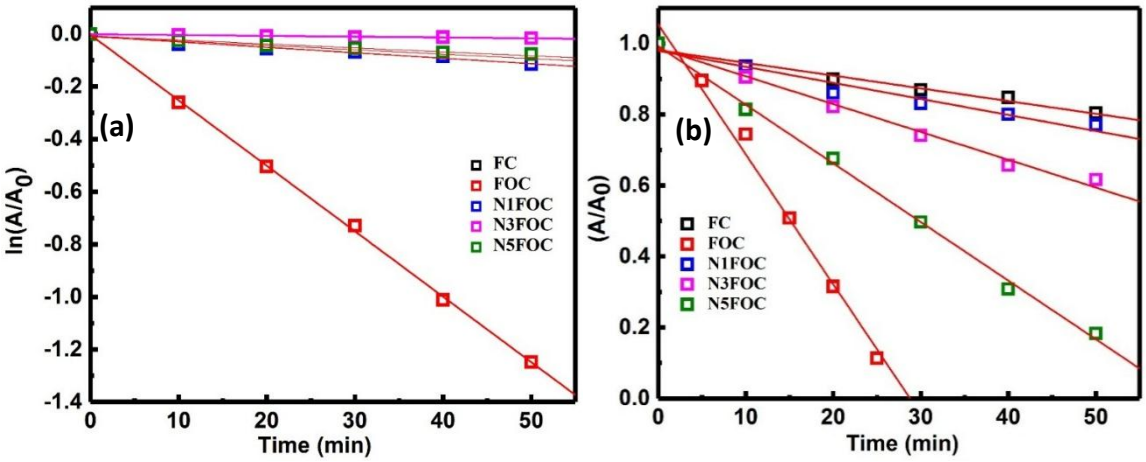

Figure 5.15: Catalytic kinetics plots of degradation of MO at λ_{max} 505 nm under (a) Fenton and (b) Photo Fenton condition.

Table 5.4: The apparent reaction rate constant for Fenton degradation and photo-Fenton degradation of MO in presence of different nanoparticles prepared in this study.

Catalyst	**Apparent reaction rate constant for Fenton degradation of MO (min^{-1})**	**Apparent reaction rate constant for photo-Fenton degradation of MO (mol $lit^{-1}min^{-1}$)**
FC	1.68×10^{-3}	3.59×10^{-3}
FOC	2.49×10^{-2}	3.36×10^{-2}
N1FOC	2.07×10^{-3}	4.52×10^{-3}
N3FOC	3.07×10^{-4}	7.84×10^{-3}
N5FOC	1.51×10^{-3}	1.65×10^{-2}

5.2.11 Possible reaction mechanism

In the following, to get a mechanistic perspective, we first discuss the possible radical based PNP and MO degradation pathway. A Fenton like reaction usually produces hydroxyl radicals by the following sequence of reactions.

$$Fe^{2+} + H_2O_2 \longrightarrow Fe^{3+} + {\cdot}OH + OH^-$$

$$Fe^{3+} + H_2O_2 \longrightarrow Fe^{2+} + {\cdot}OOH + H^+$$

$$Fe^{3+} + OH^- \rightarrow Fe^{2+} + {\cdot}OH$$

The hydroxyl (·OH) radical, a non-selective and robust oxidant, oxidizes the target pollutant. The Fenton degradation of PNP generally follows the hydroquinone route. PNP first gets oxidized into hydroquinone (HQ), which has an absorbance maximum at ~290 nm. Hydroquinone then gets further oxidized into benzoquinone (BQ) and then could be broken into smaller organic molecules. The final step is the conversion of these small molecules into carbon dioxide and water.

On the other hand, the Fenton degradation of MO produces intermediates like dimethylaniline, sodium benzenesulfonate, aniline, benzenesulfonic acid, hydroxyaniline, 4-hydroxybenzenesulfonic acid, HQ, and BQ. These intermediates then get transformed into aliphatic acids, such as oxalic acid and carboxylic acids. These compounds, in turn, are finally decomposed into CO_2 and H_2O.

In heterogeneously catalyzed Fenton reaction cycle, the Fe^{2+} (in the catalyst) gets oxidized to Fe^{3+} species due to the reduction of H_2O_2. In the next step, the oxidized Fe^{3+} ions again get reduced to Fe^{2+} by interaction with the hydroxide anion. The second step is typically

the rate-limiting one. The XRD and XPS results for all Ni substituted nanocomposites indicate the replacement of Fe^{2+} ions by Ni^{2+} in Fe_3O_4. Since the higher oxidation state of Ni (+3) is not stable enough and, therefore, the reverse reaction gets impeded in comparison to only Fe_3O_4. Hence doping FOC with Ni reduces the (dark) Fenton catalytic activity of these nanocomposites significantly.

The enhanced Fenton activity (in the dark) indicates that the FOC composite ($Fe_3C/Fe_3O_4/C$) improves the rate of the usually slower Fe^{3+} to Fe^{2+} reduction reaction. Photo-excitation of the nanocomposite also seems to facilitate this process by better charge separation. Doping FOC with Ni introduces two contrary factors in the photocatalytic degradations reported here. The first factor is the one which indicates that increased content of Ni^{2+} ions in Fe_3O_4 (i.e., in the nanocomposites) impedes H_2O_2 reduction. The second aspect is the bandgap widening due to Ni doping. It indicates that dopant energy states have possibly increased the valence bandwidth of the nanocomposite. On photo-excitation, charge transfer to the dopant additional energy states causes better charge separation than earlier. While this factor improves the photocatalytic efficiency, it still cannot compensate for the negative effect of Ni substitution of Fe in the Fe_3O_4 component of the nanocomposites.

5.3 Conclusions

In summary, we used a cost-effective and straightforward sol-gel technique to prepare various nanocomposite (e.g., Fe_3C/C, $Fe_3C/Fe_3O_4/C$, and Ni-$Fe_3C/Fe_3O_4/C$) photocatalysts for the degradation of methyl orange and p-nitrophenol in acidic medium. The XRD, XPS, TEM, and Mössbauer spectroscopy studies confirmed the formation of nanocomposites. Optimum M_S value of 68 Am^2/kg was noticed for the FC sample but decreased for FOC and NFOC

samples. The sample FOC exhibited the best apparent reaction rate constant, which indicated the high photocatalytic degradation performance under Fenton and photo Fenton conditions. Ni-doping decreases the Fenton activity (in the dark) quite significantly. The visible light photo-Fenton activity also got reduced due to Ni-doping in comparison to the FOC photo-activity. However, increasing the Ni-substitution in the FOC nanocomposites improves their photocatalytic PNP and MO degradation performances. It appears to be due to charge transfer to the dopant (Ni) energy states restricting photoexcited electron-hole recombination. Therefore, nanocomposite photocatalyst FOC and higher Ni content composite (i.e., N5FOC) samples can be explored for the removal of the MO and PNP dyes pollutants from the industrial wastewater.